Two for one: Semi-crystalline and amorphous materials via multi-temperature 3D printing from one formulation

Michael Göschl,[§,1] Dominik Laa,[$,2] Thomas Koch,[2] Evan Constable,[3] Andrei Pimenov,[3]

Jürgen Stampfl,[2] Robert Liska,[1] Katharina Ehrmann[1,*]

[$] These authors contributed equally.

[1]Institute of Applied Synthetic Chemistry, Technische Universität Wien

[2]Institute of Materials Science and Technology, Technische Universität Wien

[3]Institute of Solid State Physics, Technische Universität Wien

* Email: katharina.ehrmann@tuwien.ac.at

Abstract

Multi-material 3D printing concerns the use of two or more 3D printable materials within a single printed part. The result is a composite that benefits from the combined properties of the individual 3D printed materials. Typically, a distinct differentiation between material properties can only be achieved using multiple feedstocks and advanced engineering solutions. In this work, we create multi-material 3D printed photopolymer parts from a single monomer mixture through simple adjustments in printing temperature and light intensity. We achieve this by employing a liquid crystalline (LC) monomer that forms a highly stable LC phase in conjunction with a trifunctional thiol crosslinker. A drastic change in mechanical and optical properties was achieved depending on the presence of an LC phase during polymerization. The proof of principle from bulk experiments could be translated fully into 3D printing, achieving pixel-to-pixel resolution of the material properties solely guided by changing the printing parameters temperature and light intensity. The versatility of produced multi-material composite parts is demonstrated in shape memory applications and new methods for chemical data storage and encryption.

Graphical Abstract

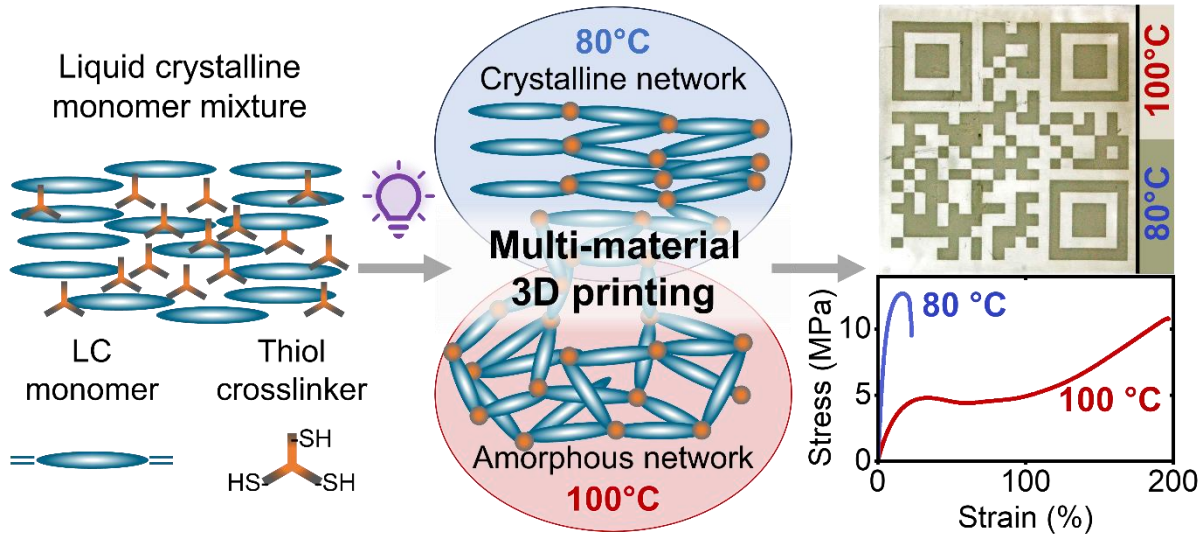

Introduction

3D printing has advanced considerably since its sole use as a prototyping method. With the advent of material diversity, 3D printing has become more widely accepted as a true alternative manufacturing method. However, in contrast to fused deposition modelling, stereolithography-based 3D printing still faces the problem that it is inherently designed to manufacture objects out of one material feed. A liquid resin mixture consisting of monomers and initiator is filled into the vat and thus determines the final polymer network properties and bulk material properties.[1] Minor adjustments in properties may be achieved by significant adjustments in curing parameters and therefore monomer conversion (grayscale printing), but the fundamental type of material (stiff vs. soft, tough vs. brittle) is determined by the type and composition of the building blocks.[2, 3] Exchanging the material feed, i.e. the vat, is time intensive and challenging for precise spatio-temporal control of the process.[4] Additionally, vat exchanges bear the problem of contaminating the different, sticky resins with each other, affecting the final quality of a printed object. Instead of exchanging the material feed, its composition can also be changed during printing (gradient printing).[5] This allows for some more freedom in the types of properties differentiated. For example, varying degrees of crystallinity could be obtained through such an approach.[6] However, this limits the multi-material property differentiation to a property gradient along the printing direction. Additional difficulties may arise in homogenizing the gradually changing resin composition of the typically rather viscous resins during the printing process.

Therefore, more recent multi-material vat photopolymerization strategies have focused on the change of material properties through the change in irradiation conditions, light intensity and light colour.[4] In greyscale printing (in analogy to a black-and-white printer), the intensity of the light source is varied to alter the conversion of the resin into the polymer network and thereby alter its thermomechanical behaviour. Hard and soft sections within one object have been fabricated from (meth)acrylate resins at high and low irradiation intensities, respectively, by simply changing the conversion.[7, 8, 9] However, postcuring may increase the conversion of unreacted monomer, which could not be washed out of a bulk object, in undercured areas. Hence, the property differentiation decreases. Alternatively, uncatalyzed cycloaddition

dimerization reactions of multifunctional prepolymers led to high-resolution stiffness tuning without decreasing the property differentiation during post-curing. This effect is based on the drastically decreased probability of bond dissociation in the degradation motif if it is embedded in a highly rigid matrix. In a variation of this approach, light-stabilized dynamic materials based on photocycloaddition reaction of a prepolymer and a crosslinker have been utilized to induce tunable degradation below a certain crosslinking density at lower laser energies for 3D printing and entirely undegradable objects above a certain crosslinking threshold at high laser energies.[10] Another property differentiation is based on dye oxidation at high radical concentrations due to high irradiation intensities opposite non-oxidized dye at low intensity.[11]

In contrast to greyscale printing approaches, multi-colour printing, or multi-wavelength printing (in analogy to a colour printer), refers to 3D printing strategies where different colours (for 3D printing with LED light sources utilizing digital light processing) or wavelengths (for laser-stereolithography) are utilized to address (semi-)orthogonal polymerization reactions during the printing process.[12, 13, 14, 15] Most frequently, semi-orthogonally triggered radical photoinitiators, which respond to visible and UV light, and photoacid generators, which respond to UV light only, are reported to differentiate hard and soft material sections in one printed object.[16] This combination of initiators allows to selectively cure a soft (meth)acrylate network in the visible light region and a much stiffer interpenetrating network consisting of said (meth)acrylate network and an epoxy-network simultaneously in the UV light region.[17, 18] Further studies have added post-modification steps to this approach to vary the dangling chain ends in the soft network.[19] Most greyscale and multi-color/wavelength printing approaches limit the property differentiation to stiff/soft,[13, 14, 15, 16, 17, 18, 19] although some new property types have been introduced recently. For example, the semi-orthogonality of photoacid generators to radical photoinitiators utilized for printing have recently been employed to modulate the pH of the formulation with spatiotemporal control, which was exploited for the change of material color for pH-sensitive additives.[20] Another recent report also demonstrates degradable/non-degradable material properties from one resin. In this case, two chromophore-based prepolymers, are mixed with each other and cured under conditions, which allow the fully orthogonal deposition of either polymer network without the other one onto the printing platform.[21] There is, however, one limitation common to all of these approaches: The final object will contain uncured monomers or prepolymers, which, depending on the crosslinking density, cannot be washed out during the post-processing step. This is particularly problematic because the latent photoinitiators are still in the network and may cure leftover monomers over the lifetime of an object, thereby diminishing the intended property differentiations. In case of (meth)acrylate formulations, even autoinitiation may be sufficient for this process. In other cases, the monomers may slowly diffuse out of the object, causing issues like cavities, sticky surfaces and the release of potentially hazardous monomers.

Therefore, we suggest a paradigm change in multi-material printing by rethinking the approach of obtaining varying material properties from a selection of monomers. Instead of ascribing different material properties to different monomers, we envision “switchable monomers”, which change their functionality based on the printing parameters, thereby affecting the obtained material properties.

Herein, we propose the printing temperature as a new parameter to alter the material properties mid-printing. We suggest our recently established liquid crystalline thiol-ene monomer platform[22] as a means to affect crystallinity of resulting polymer networks via the printing temperature instead of previously utilized property tuning via alignment through rubbed polymer surfaces, stretching of prepolymers, or external fields.[23, 24] While 3D printing at moderately high temperature (80 °C) enables trapping of the liquid crystalline state of the formulation in the network, rendering it stiff and opaque, printing at higher temperature (>95 °C) allows for curing of largely amorphous polymer networks from the formulation's isotropic state. Based on this approach we optimize the property differentiation through finetuning the irradiation protocol (intensity, duration) to highly precise multi-material property printing, with pixel-to-pixel precision property switching within one printing layer, demonstrating first suggestions for application as smart materials for shape memory and chemical data storage and encryption.

Property differentiation studies

Stereolithography-based 3D printing typically requires fast gelation of a polymer formulation, which is achieved through network formation. Since polymer networks traditionally exhibit amorphous and inhomogeneous microstructures, however, it is particularly difficult to influence the polymer properties via the materials' microstructural architecture.[22] We have recently demonstrated 3D printing of liquid crystalline formulations, which contain high amounts of the evenly distributed LC motif in the main chain of the polymer network by polymerizing a liquid crystalline diene with a trithiol via thiol-ene photopolymerization.[22] This has facilitated uniform and irrevocable formation of crystallinity throughout the material. However, property differentiation via printing parameters could not be achieved. Therefore, another liquid crystalline ene-monomer, which exhibits an even more highly ordered smectic X phase, was envisioned and paired with a trifunctional thiol in a photoreactive formulation. Polarized optical microscope analysis of the formulation revealed an exceptionally stable LC phase ranging from approximately 79 to 109 °C (Figure 1A, Supplementary Figure 2), which is present at nearly identical temperatures as the pure monomer (77 to 111 °C).[25]

According to our previous study, the formulation's LC temperature range, which is largely influenced by the monomer's LC phase stability, strongly correlates with its ability to form a crystalline, mechanically strong polymer network. To exploit 3D printing from the liquid crystalline state for multi-material 3D printing, precise switching of the formulation's state between liquid crystalline and isotropic liquid is required. Compared to previously reported monomers, the present monomer combination exhibited a much sharper transition between its LC and isotropic phases than any previous formulation, enabling it to be polymerized from either of these phases with a simple temperature adjustment.

Indeed, during initial tests, irradiation of the molten formulation at 80 °C resulted in opaque, stiff polymer specimens, indicating significant crystallization. Moreover, we succeeded in producing transparent, amorphous specimens by raising the temperature to 110 °C before irradiation (Figure 2A). This property-switchable behaviour gave rise to the development of the concept of crystallinity-based multi-material printing from a single formulation (Figure 1B). By dynamically changing the temperature during the 3D printing process, crystallization can be

induced or avoided deliberately. By applying this principle within a single print layer, full 3D control of mechanical and optical properties in a printed part could be achieved.

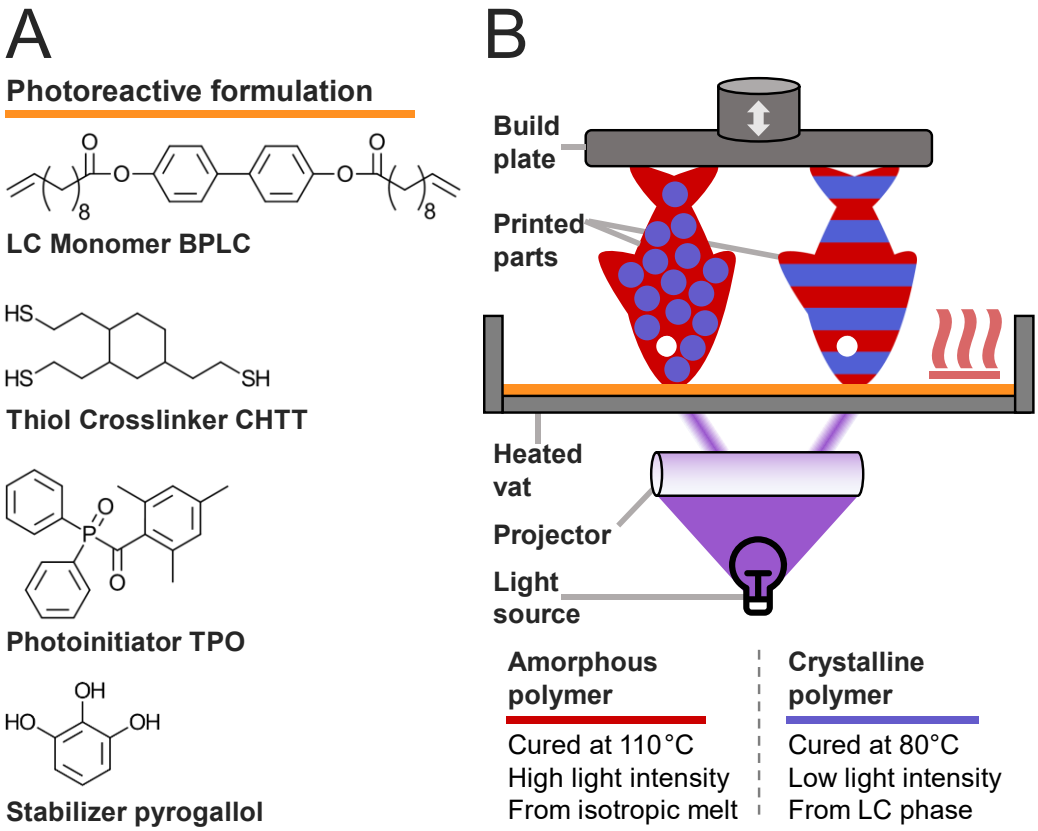

Figure 1: Concept of multi-material 3D printing from a single formulation. A) Photoreactive formulation containing difunctional liquid crystalline terminal alkene monomer BPLC, trifunctional crosslinker CHTT, photoinitiator TPO, and stabilizer pyrogallol. B) A heated DLP (digital light processing) 3D printer is programmed to irradiate certain areas of each printed layer at a higher temperature and irradiation intensity, and other areas at a lower intensity and temperature. A photoreactive formulation consisting of the biphenyl-based liquid crystalline monomer BPLC and trithiol crosslinker CHTT along with a photoinitiator and stabilizer is employed. At 80 °C, the formulation is present in the liquid crystalline phase, which causes crystalline domains to be incorporated into the polymer network, leading to an opaque appearance, and enhanced strength and stiffness. At 100 °C, the formulation is present as an isotropic molten phase, which, upon polymerization, turns into a transparent, soft, amorphous material.

The variability of crystallinity is highlighted by dynamic scanning calorimetry (DSC) measurements, which indicate endo- and exothermal phase transitions in materials upon controlled heating (Figure 2B). The softer, amorphous network is characterized by a baseline shift associated with the glass transition temperature (T_g) and a broad, flat peak around 100 °C that could signify traces of crystallinity. For the samples cured at 80 °C, we found that crystallinity could be maximized by employing a mild two-step irradiation procedure, in which a low-intensity irradiation step slowly initiates polymer network formation, followed by a high-intensity second irradiation step that finalizes the curing process. In this case, a strong melting peak (T_m) occurs around 150 °C. If the mild first irradiation step is avoided and the strong final irradiation step is employed immediately, the melting peak is severely diminished, and the DSC curve more closely resembles the amorphous specimen. Macroscopically, the sample is still opaque. The benefit of the initial low-intensity irradiation step on enhancing crystallinity may

be twofold: Firstly, the avoidance of heating the sample excessively during polymerization (through heat of polymerization and the light source itself) ensures that the liquid crystalline phase is maintained, from which polymer crystallinity is formed. This effect could be proven through a multi-material irradiation attempt producing crystalline and amorphous materials solely by changing the irradiation intensity while keeping the temperature constant (Figure 3A). Secondly, it is possible that with high-intensity irradiation, the crosslinking process takes place faster than crystallization, immobilizing the polymer network before the polymer chains can align. Along with the T_g, a broad and flat peak around 100 °C could indicate a separate type of crystallinity, potentially featuring smaller crystallite sizes or crystallization associated with a different alignment of the polymer chains. The material's degree of crystallinity D_C results in a fundamental difference in mechanical properties as seen during dynamic mechanical analysis (DMA), where the storage and loss modulus of a material are determined as a function of temperature (Figure 2C). Herein, the crystalline network's storage modulus is not significantly impacted by the glass transition around 25 °C. Instead, the storage modulus, which serves as a strong indicator for a polymer's stiffness, stays relatively constant and starts to diminish only at 100 °C.

Finally, we reveal the material's excellent tunability using tensile testing (Figure 2D). While the highly crystalline specimens exhibit high stiffness and an ultimate tensile strength around 12 MPa, the amorphous material exhibits pronounced yielding and strain hardening, finally resulting in an elongation at break of over 200% and strength at break around 10 MPa. Thus, with no change in formulation composition and only a simple temperature adjustment, fundamentally different materials can be created.

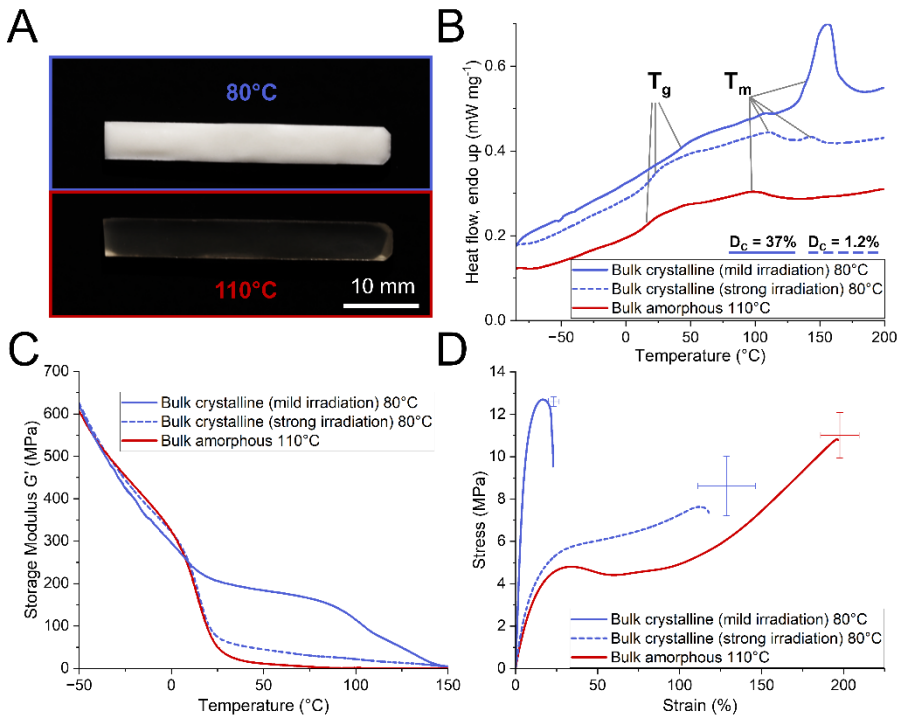

Figure 2: Demonstration of highly variable material properties of bulk cured specimens depending on curing conditions (curing temperature: 80 °C vs. 110 °C; mild irradiation: 300 s at 1.5 mW cm^{-2} followed by 180 s at 290 mW cm^{-2}; strong irradiation: 180 s at 290 mW cm^{-2}). A) sample transparency, B) differential scanning calorimetry (DSC) with degrees of crystallinity D_C, and thermomechanical properties from C) dynamic mechanic analysis (DMA) and D) tensile tests.

3D printing in and outside the liquid crystalline temperature range

Next, we translated the manufacturing of different parts with distinct material properties from one formulation from bulk curing conditions to 3D printing, utilizing different printing temperatures. In an initial test, the layers were irradiated at two different irradiation settings along a temperature gradient from 78 °C to 110 °C (Figure 3A). The same total light dose was emitted for each layer, with one half irradiated for 4.7 s at 80 mW cm^{-2} and the other half irradiated for 24 s at 15.75 mW cm^{-2}. Analysis of the cross-section of the printed part using polarized optical microscopy revealed relatively sharp cutoffs between bright crystalline and dark amorphous sections at 85 °C (high intensity) and 87 °C (low intensity). Additionally, one layer printed at 82 °C did not crystallize when using high irradiation intensity. Therefore, the milder irradiation setting was used to reliably print crystalline specimens. The bright phenomena above 100 °C are directional traces of the microtome cut and not crystalline sections, which appear on different areas depending on the angle of the slice compared to the polarizing filters. The experiment also serves as a proof of principle for crystallinity manipulation using greyscale printing only, without changing the printing temperature. Using an accurately defined temperature, in this case 85 to 86 °C, crystallinity could be induced or avoided without a change of temperature and simply by changing the irradiation intensity.

Fully crystalline and fully amorphous printed specimens made it evident that the multi-material effect can be achieved just as pronounced as in bulk during printing (Figure 3B). The printing temperature of 110 °C, which was chosen for the isotropic liquid formulation state, resulted in relatively weak, soft specimens, some of which exhibited cracks upon removal from the platform. To explore this behavior further, an additional printing temperature of 100 °C was chosen, which also resulted in transparent specimens which were more resilient. Three printing temperatures were evaluated: 80 °C for printing from the liquid crystalline regime, 110 °C for printing from the isotropic melt, and an intermediate temperature of 100 °C, still within the LC phase but resulting in a transparent specimen. DSC of the samples printed at 80 and 100 °C revealed distinct melting peaks (Figure 3C), which imply significant degrees of crystallinity D_C (34% and 22%, respectively, Supplementary Table 1). In addition to the lower D_C, a melting point depression of 35 °C occurred for specimens printed at 100 °C compared to those printed at 80 °C. The sample printed from the isotropic state at 110 °C exhibited some minor endothermic heat flow over a broad range from 75 to 100 °C, indicating only traces of crystallinity, which likely occur due to small-scale alignment of oligomeric thiol-ene prepolymers, that cannot arrange into larger crystalline domains. Such crystallites with a melting point of 100 °C only demonstrate a small impact on the sample's stiffness in dynamic mechanical analysis. Compared to these specimens, the sample printed at 80 °C exhibits increased stiffness due to crystallinity, maintaining a high storage modulus between room temperature and 100 °C (Figure 3D). Finally, tensile tests also confirmed a much higher stiffness of the semicrystalline specimens 3D printed at 80 °C compared to samples printed at 100 and 110 °C (Figure 3E). Compared to the bulk cured crystalline sample, only slightly lower tensile strength was achieved while the elongation at break was doubled. While the amorphous specimens printed at 110 °C did not achieve satisfactory results compared to the amorphous bulk polymer, the adjustment to 100 °C printing temperature produced a soft, yet tough polymer. Printing of a five-layer composite structure, where the layers are printed in turns at

80 and 100 °C, gave the same melting temperature region in DSC measurements compared to the samples entirely printed at 80 °C, albeit with a smaller signal. This indicates that the layered structure did not impede the formation of crystalline and amorphous material properties in adjacent layers. The tensile properties of the composite structures were found to be between the amorphous and crystalline samples, which verifies good layer adhesion between crystalline and amorphous layers and demonstrates the capability for property tuning through multi-material printing.

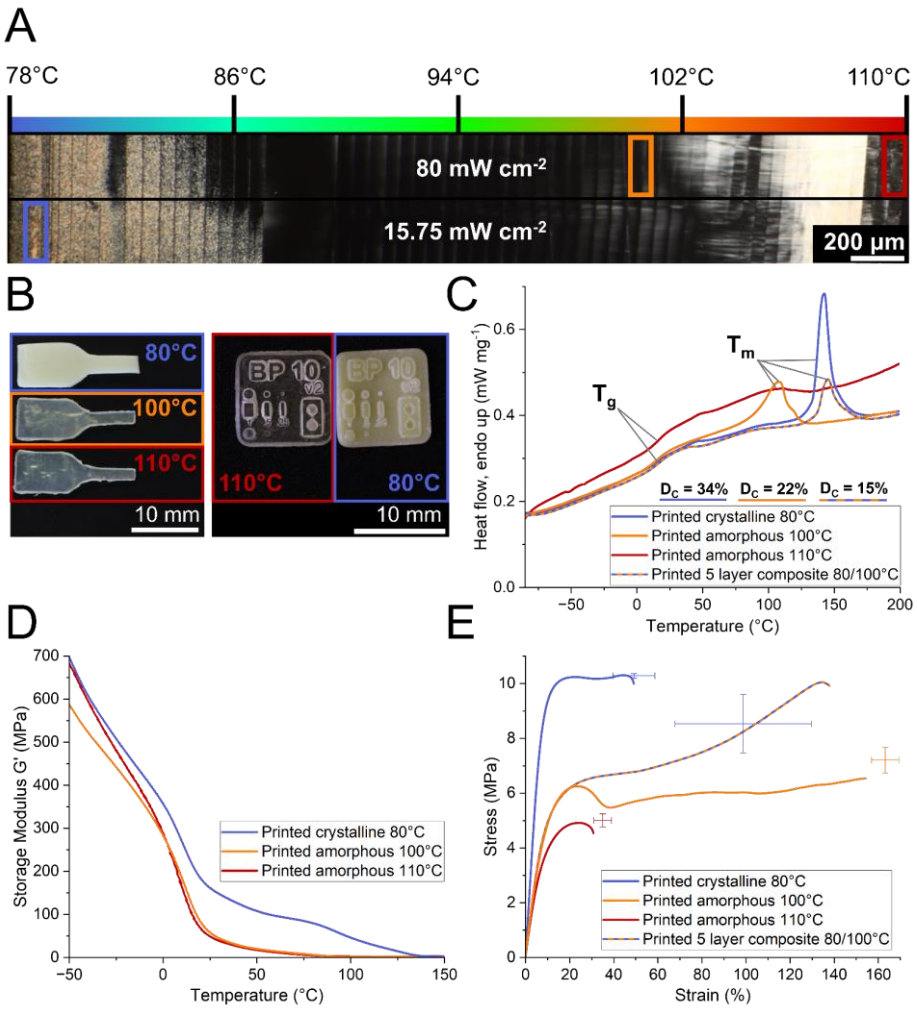

Figure 3: Variation of material properties in printed parts depending on curing conditions. A) Polarized optical microscope image of a 10-µm cryo-microtome cut of a polymer specimen cured at two different light intensities and irradiation times (4.7 s at 80 mW cm^{-2} and 24 s at 15.75 mW cm^{-2}, same total light dose) through a temperature gradient. The bright phenomenon between 105 and 108 °C is caused by the tracing of the microtome knife. For B-E, the curing temperature was varied between 80 °C, 100 °C and 110 °C. For the amorphous samples the more intense, short irradiation program was selected, while for the crystalline specimens the slower, mild irradiation program was used. B) Sample transparency, C) crystallinity measured by dynamic scanning calorimetry (DSC) with degrees of crystallinity D_C, and thermomechanical properties from D) dynamic mechanic thermal analysis (DMA) and E) tensile tests. Additionally, E) showcases the tensile test results of a five-layer composite sample, in which two amorphous layers are encased between crystalline layers.

We tested the formulation's capabilities to be 3D printed into a complex hollow pyramid shape. As this experiment required an extended amount of time due to the specimen's number of

layers, we adjusted the composition of the formulation by adding a larger amount of the radical stabilizer pyrogallol. We compensated for the loss in reactivity by slightly increasing the amount of the photoinitiator TPO. This adjustment, along with an intermediate printing temperature of 90 °C, caused slight crystallinity to occur in the pyramid, making it semi-opaque. Layer formation throughout the printing process was successful and resulted in an even and distortion-free formation of the pyramid shape (Figure 4A). While minor overpolymerization was observed on certain areas of the inside of the beams, the scanning electron microscope image demonstrates pixel-perfect curing and even layer dimensions and spacing.

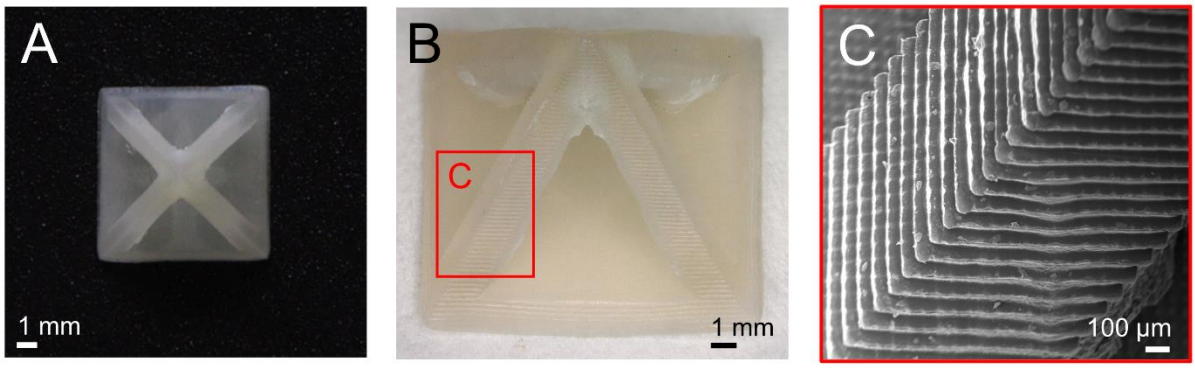

Figure 4: Printed hollow pyramid specimen showcasing excellent resolution and layer formation of the printed parts. A formulation containing an increased amount of the stabilizer pyrogallol was printed into a challenging "additive manufacturing only" hollow pyramid shape with a 7x7 mm baseplate.

Multi-property printing

After the successes in modulating the transparency and mechanical properties during the printing process, we expanded the technique to produce structures with the two distinct material properties in each layer. The process to print a layer begins by preheating the build plate and the vat to 100 °C for curing the amorphous phase of the material. Subsequently, the build plate is lowered into the vat and the amorphous sections are cured selectively. This is followed by peeling the solidified layer from the vat. Before repeating the process for the crystalline phase, the build plate and vat are cooled to 80 °C.

To demonstrate the precise spatial control over the material properties, we printed a QR code (Figure 5A). For imaging, transmitted light microscopy was utilized, in which amorphous sections appear white due to transmitted light and crystalline sections appear dark because the light cannot penetrate the sample. The inclusion of the QR code was chosen to show the fine control over the material properties. Visual inspection of the 3D printed part under transmitted light microscopy shows that the material properties can be defined for each printed voxel (volumetric pixel). Each voxel has the size of 50x50x50 μm^3 according to the capacities of the DLP light engine with a pixel pitch of 50 µm and a layer height of 50 µm. The magnified detail clearly showcases that the definition of the material property per voxel is possible. Additionally, we illustrate a 3D printed "body with skeleton" model with a fine-grained control over the material properties (Figure 5C). For this part, an encapsulation of the intricate details of the skeletal model was achieved by embedding the layers strategically with layers of amorphous material. The two magnified detail images show that the transparency of the

amorphous layer exhibits minimal obscuration of the fine details inside the model. Using this technique, composite structures can be manufactured. Figure 6B and D showcase the capability of this printing technique to produce composite structures of any desired geometry and soft/hard material composition, of which the layered composite was tensile tested (Figure 3E).

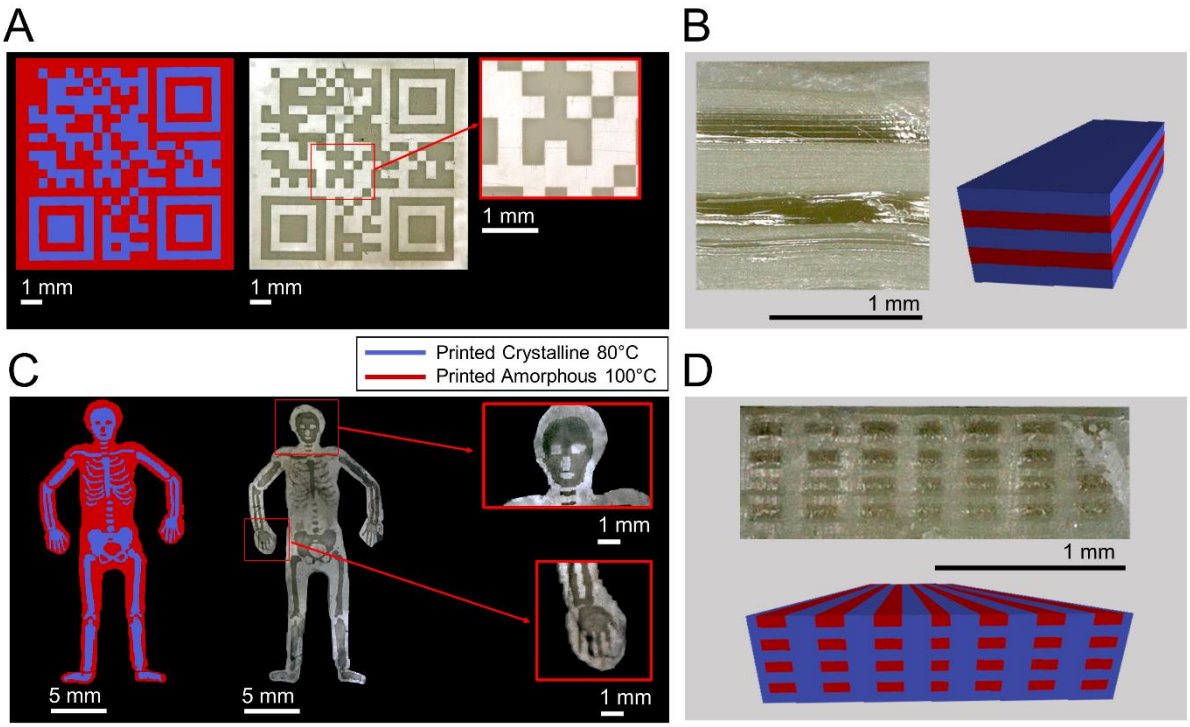

Figure 5: Samples of 3D printed parts with different material properties depending on the curing conditions. A) Digital design of a QR code, the 3D printed object visualized under transmitted light microscopy, and a magnified detail of the printed code. B) Cross section of a 3D printed five-layer tensile test specimen with three crystalline and two amorphous layers and the 3D design corresponding to the printed specimen. C) Digital design of a skeletal model with two properties, its overall appearance under transmitted light microscopy, and magnified details of the head and hand regions. D) 3D printed cross section of a fiber structure with amorphous toughening elements in the crystalline base structure and visualization of the corresponding voxel-based design.

Functional applications

The unique combination of tunable mechanical properties and the simultaneous presence of crosslinking and crystallinity opens many smart material applications for this monomer combination. Shape memory behavior was confirmed by cyclic testing using a dynamic mechanical analysis instrument (Figure 6A). Herein, we performed a total of 30 cycles of heating, elongation to 50% strain, cooling, shape fixity evaluation by releasing tension and shape recovery by heating under no tension. The shape fixity ratio demonstrates the material's ability to be fashioned into an arbitrary shape without reverting back to its original shape in the absence of the shape recovery stimulus, (here: temperature increase). The specimens expanded slightly upon cooling, which points to a negative thermal expansion coefficient due to crystallization from the elongated state, as reported previously for liquid crystalline polymer networks.[26] This expansion compensates for the contraction that usually occurs upon cooling, finally resulting in a "slightly above perfect" average shape fixity ratio of 100.8%. The shape recovery ratio is the percentage of elongation recovered by heating the specimen to its

crystallite melting point.[27] Surprisingly, the so-called training phenomenon, which typically gives a worse shape recovery during the initial cycles, did not occur at all as already in the first cycle, 99.8% recovery of the initial shape was achieved. Throughout all 30 measured cycles, an outstanding average recovery rate of 99.7% was achieved.

With the unique capability of crystallinity control during 3D printing, specimens with crystalline, shape-imprintable and recoverable sections can be created, while other sections are deliberately left amorphous. Hereby, smart micro-devices can be fabricated without the need to join different materials through mechanical or chemical techniques. A proof of concept is presented in Figure 6B, where a printed part has a crystalline joint section and the rest of the part is amorphous. By heating the object, the crystalline joint was bent to the desired angle, which is fixed upon cooling to room temperature. Upon heating the sample again, the initial shape was recovered.

Beyond the use of the monomer combination's tunable thermomechanical properties, the adjustable optical attenuation in the visible range of light, which is four times greater in the crystalline phase ($\boldsymbol{\alpha}$ = 10640 m^{-1}) than in the amorphous phase ($\boldsymbol{\alpha}$ = 2680 m^{-1}, Supplementary Figure 3) presents options for parameter-dependent encoding of information. For example, this could be applied in the form of a multi-material printed heat warning sign that only becomes visible above a certain temperature (Figure 6C). Herein, a crystalline top layer renders the sign indiscernible at room temperature. Another advanced application would be encrypted chemical information storage. For this application, we printed a five-layered part that consists of a QR code obscured by crystalline layers and insulated by amorphous layers (Figure 6D, Supplementary Video). At room temperature, the code is invisible and can only be revealed by placing a glass lid on top of the printed part and heating the lid. This enables a targeted heat transfer to the top layer of the part, causing it to turn isotropic and rendering the code readable (Supplementary Video). When heat is applied without the correct set of instructions (too harshly or not specifically at the top layer, i.e., in an oven or with a heat gun without a glass lid), parts of the QR code also disappear, rendering it impossible to scan and thereby increasing data storage security.

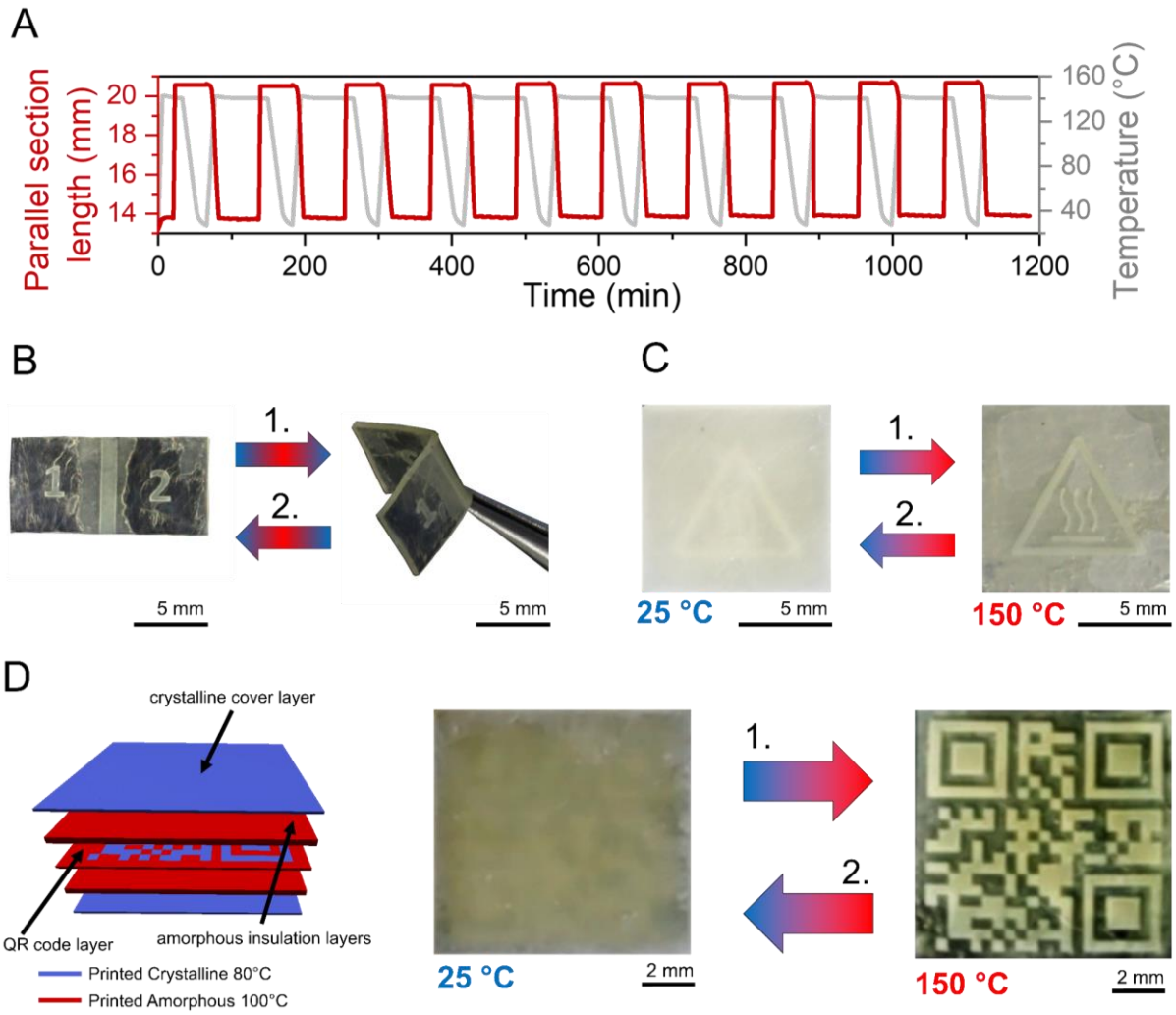

Figure 6: Potential of the material to be used for stimuli-responsive functional applications. A) Cyclic shape memory testing of a bulk cured specimen exhibiting near-perfect shape fixity and shape recovery. B) A 3D printed shape memory part that exhibits shape programmability in a defined crystalline area. C) A 3D printed heat warning sign is revealed at high temperature due to the melting of crystallites in a thin 3D printed layer and obscured again when cooled. D) 3D printed part that illustrates the process of storing data with the help of controlled formation of crystalline and amorphous material. The cross-sectional view of the voxel-based model of the printed structure shows a QR-code layer, crystalline cover layers, and amorphous insulation layers in-between. At room temperature (25 °C) no QR code is visible due to the crystalline cover layer. When the top layer is evenly heated to 150 °C, the QR code is revealed. Removing the heat source causes the part to change back to its uniform opaque appearance.

Conclusion

The ability to program mechanical and optical properties freely in three-dimensional space holds great potential for highly advanced applications. We present a noncomplex photopolymerizable system, which, through a simple printing parameter adjustment, can be cured to yield radically different materials by selectively translating a liquid crystalline phase into a semicrystalline polymer network. We were able to fully reproduce and enhance the results of the bulk material study in a 3D printer by depositing voxel-accurate crystalline and amorphous polymer sections in 3D. Thus, we established multi-material printing from a single formulation, which we used to create composite layer and fiber structures, shape memory materials, and parts capable of storing and selectively displaying encrypted information. First

smart applications of this monomer system have been explored in this work, and we believe that the principle may be translatable to other monomer systems to further expand the scope of applications.

Methods

Monomer synthesis

4'-(9-Decenylcarbonyloxy)-4-biphenylyl 10-undecenoate (BPLC) was prepared according to Imae et al. from 4,4'-dihydroxybiphenyl and 10-undecenoyl chloride catalyzed by triethyl amine.[28] After purification by recrystallization, 34.05 g (92%) of the product were isolated.

1,2,4-Cyclohexanetriethanethiol (CHTT) was synthesized in analogy to our previous work.[22]

Formulation preparation and analysis

To prepare the photopolymerizable liquid crystalline monomer formulation, 0.2 wt% (based on total formulation weight) of the inhibitor pyrogallol and 1 mol% (based on terminal double bonds) of the photoinitiator diphenyl (2,4,6-trimethylbenzoyl)- phosphine oxide (TPO) were weighed into a brown glass vial. Next, the trifunctional thiol CHTT was added, the mixture was heated to approximately 50 °C and stirred well using a vortex mixer. Lastly, the liquid crystalline monomer BPLC was added, and the mixture was heated to approximately 120 °C (isotropic melt) and homogenized using a vortex mixer by stirring for approximately two minutes. A molar ratio of 1.5 to 1 of BPLC to CHTT was used to ensure an equimolar amount of reactive terminal alkene and thiol groups. The formulation's melting point and liquid crystalline behavior were analyzed using polarized optical microscopy.

Bulk polymer curing

Bulk polymer specimens for tensile tests and dynamic mechanical analysis were cured in a custom-built heated mold, which enables accurate temperature control.[22] The formulation was poured into approximately 2-mm thick molds cast from silicone. The mold was preheated to 80 °C for crystalline polymer synthesis, and to 100 °C for amorphous polymer synthesis. For the "mild irradiation" crystalline specimens, an initial irradiation step was conducted by irradiating the formulation for 300 s at 1.5 mW cm^{-2} using a 405 nm LED light source. Afterwards, a second irradiation was employed at 290 mW cm^{-2} for 180 s using a 365 nm LED light source. For the "strong irradiation" and amorphous specimens, only the second step was used. The irradiation steps were repeated after the specimens were carefully turned upside down and placed back into the mold.

3D printing

3D printing was performed using stereolithography (SLA) with a digital light processing (DLP) light engine (up to 80 mW cm^{-2}, 385 nm). The used prototype printer employs independent control of vat, building platform and vat frame. Depending on the desired material properties the temperatures of the vat and building platform were adjusted. For experiments in this work, temperatures between 78 and 110 °C were used. The vat frame was kept at a constant temperature of 80 °C. For each print layer, the building platform was lowered to the vat keeping a 50 µm-high section coated with the liquid formulation. To achieve parts with multiple properties within a single layer we first cured the crystalline sections at 80 °C at a lower

irradiation intensity applied over a longer time (24 s at 15.75 mW cm^{-2}). Afterwards, the temperature was changed, and the amorphous sections were cured, for which a higher irradiation intensity was used (4.7 s at around 80 mW cm^{-2}). After each curing step, the part was peeled off the vat by lifting the build plate, which allows for more of the formulation to flow under the previously printed material. The process was repeated until the part was finished. With a voxel-based modelling software we were able to create multi-material objects that were then saved as a set of images, wherein each pixel corresponds to one voxel. To print different properties, the printer uses one of these images for each layer. Depending on the color of each pixel the software was programmed to detect which material property should be printed and chooses the right printing condition. Post-processing of parts was performed by submerging the part in toluene and sonication for up to five minutes at around 35 °C. The crystalline parts were sonicated for 4-5 minutes, while the amorphous parts were sonicated for 2-3 minutes due to their lower solvent resistance and typically slightly less unpolymerized residue than the crystalline parts.

Polymer characterization

To perform differential scanning calorimetry (DSC), 3-5 mg of the polymer networks were weighed into aluminium DSC crucibles and first cooled to -90 °C, after which they were heated to 200 °C. Thereafter, the cooling and heating cycle was repeated. Heating and cooling rates of 10 K min^{-1} were used. For the measurements displayed in this article, the first heating cycle was used, since the second cycle displayed minor shifts in the crystallite melting points after being heated to 200 °C. Therefore, we considered the first cycle to be more representative of the polymer network present at room temperature after curing. Crystallinity calculations from the obtained enthalpies are described in the Supplementary Information (Supplementary Table 1).

For dynamic mechanical analysis (DMA), cuboid samples according to DIN EN ISO 6721 were cured in bulk and using 3D printing as described previously. The bulk specimens were lightly sanded to correct geometric irregularities. The samples were clamped into rectangular fixtures and subjected to torsional shear strain of 0.1% with a frequency of 1 Hz through a temperature range of -50 to 200 °C with a heating rate of 2 K min^{-1}.

To measure tensile tests, dogbone shape specimens according to ISO 527 test specimen 5b were cured in bulk and using 3D printing as described previously. The bulk specimens were lightly sanded to correct geometric irregularities. Tensile tests were performed with a traverse speed of 5 mm min^{-1}.

Cryo-microtome cuts of the temperature gradient 3D print were performed using a glass knife at a thickness of 10 µm at -80 °C.

Polarized optical microscopy was used to analyze the liquid crystalline phase present in the formulations and the temperature gradient 3D print.

To analyze printed specimens, digital light microscopy using depth composition was used in reflected light and transmitted light mode.

Scanning electron microscopy images were recorded with an electron high tension voltage of 10.00 kV at a working distance of 12.12 mm.

Cyclic shape memory tests were performed on dogbone shape specimens in analogy to those used in tensile tests. The specimens were fastened into a dynamic mechanical analyser equipped with a rectangular fixture. First, the samples were heated to 140 °C using a heating rate of 20 K min^{-1}. After an equilibration period of 15 min, they were strained until the parallel section of the specimen had reached 50% elongation. Next, the samples were cooled to room temperature using air cooling with a cooling rate of 5 K min^{-1}. At room temperature, the tension applied by the instrument was released to measure the resulting contractive or expansive response of the samples, from which the shape fixity ratio was calculated. To test the shape recovery, the samples were again heated to 140 °C using a heating rate of 10 K min^{-1} under no external stress, where they were held for 60 min. To calculate the shape recovery ratio, the contraction of the samples during this heating process was divided by their sample strain after being allowed to contract upon releasing the instrument's tension. After contracting for 60 min, the process was repeated by straining the sample again. A single sample was subjected to three measurements of ten cycles each. The shape fixity and shape recovery ratios were calculated using Supplementary Equations 2 and 3.

The multi-material shape memory part (Figure 6B) was shape imprinted by bending it at the crystalline middle section and briefly heating it to 150 °C using a heat gun and cooling it back to room temperature, upon which the new shape was fixed. By heating the part to 150 °C again, the original flat shape was recovered.

The temperature warning sign (Figure 6C) was set up by placing a microscope glass slide under and over the printed warning sign. The printed part was placed on top, and another glass slide was used to cover the printed part. The specimen was heated using a heat gun.

The concealed QR code (Figure 6D) was revealed by placing a glass slide on top of the specimen and heating it with a heat gun evenly from above. Below the specimen, a metal plate was placed to ensure a heat sink effect.

Data Availability Statement

The data supporting this article have been included as part of the Supplementary Information. Data for this article beyond the scope of the Supplementary Information, including raw data of all presented graphs, are available at TU Wien Research Data at https://doi.org/10.48436/drx13-s7537.

Author Statement

Michael Göschl: Methodology, Validation, Formal Analysis, Investigation, Data Curation, Writing – Original Draft, Writing – Review & Editing, Visualization **Dominik Laa:** Methodology, Software, Validation, Formal Analysis, Investigation, Writing – Original Draft, Writing – Review & Editing, Visualization **Thomas Koch:** Methodology, Formal Analysis, Investigation, Writing – Review & Editing **Evan Constable:** Methodology, Formal Analysis, Investigation, Writing – Review & Editing **Andrei Pimenov:** Formal Analysis, Writing – Review & Editing **Jürgen**

Stampfl: Formal Analysis, Resources, Writing – Review & Editing, Supervision, Funding Acquisition **Robert Liska:** Formal Analysis, Resources, Writing – Review & Editing, Supervision, Funding Acquisition **Katharina Ehrmann:** Conceptualization, Methodology, Validation, Formal Analysis, Investigation, Data Curation, Writing- Original Draft, Writing – Review & Editing, Visualization, Supervision, Project Administration

References

1. Nazir A, Gokcekaya O, Md Masum Billah K, Ertugrul O, Jiang J, Sun J*, et al.* Multi-material additive manufacturing: A systematic review of design, properties, applications, challenges, and 3D printing of materials and cellular metamaterials. *Materials & Design* 2023, **226:** 111661.

2. Kuang X, Wu J, Chen K, Zhao Z, Ding Z, Hu F*, et al.* Grayscale digital light processing 3D printing for highly functionally graded materials. *Science Advances* 2019, **5**(5)**:** eaav5790.

3. Wang B, Engay E, Stubbe PR, Moghaddam SZ, Thormann E, Almdal K*, et al.* Stiffness control in dual color tomographic volumetric 3D printing. *Nature Communications* 2022, **13**(1)**:** 367.

4. Shaukat U, Rossegger E, Schlögl S. A Review of Multi-Material 3D Printing of Functional Materials via Vat Photopolymerization. *Polymers* 2022, **14**(12)**:** 2449.

5. Wang H, Xia Y, Zhang Z, Xie Z. 3D gradient printing based on digital light processing. *Journal of Materials Chemistry B* 2023, **11**(37)**:** 8883-8896.

6. Rylski AK, Maraliga T, Wu Y, Recker EA, Arrowood AJ, Sanoja GE*, et al.* Digital Light Processing 3D Printing of Soft Semicrystalline Acrylates with Localized Shape Memory and Stiffness Control. *ACS Applied Materials & Interfaces* 2023, **15**(28)**:** 34097-34107.

7. Peterson GI, Schwartz JJ, Zhang D, Weiss BM, Ganter MA, Storti DW*, et al.* Production of Materials with Spatially-Controlled Cross-Link Density via Vat Photopolymerization. *ACS Applied Materials & Interfaces* 2016, **8**(42)**:** 29037-29043.

8. Valizadeh I, Al Aboud A, Dörsam E, Weeger O. Tailoring of functionally graded hyperelastic materials via grayscale mask stereolithography 3D printing. *Additive Manufacturing* 2021, **47:** 102108.

9. Yue L, Macrae Montgomery S, Sun X, Yu L, Song Y, Nomura T*, et al.* Single-vat single-cure grayscale digital light processing 3D printing of materials with large property difference and high stretchability. *Nature Communications* 2023, **14**(1)**:** 1251.

10. Gauci SC, Ehrmann K, Gernhardt M, Tuten B, Blasco E, Frisch H*, et al.* Two Functions from a Single Photoresist: Tuning Microstructure Degradability from Light-Stabilized Dynamic Materials. *Advanced Materials* 2023, **35**(22)**:** 2300151.

11. Peng X, Yue L, Liang S, Montgomery S, Lu C, Cheng C-M*, et al.* Multi-Color 3D Printing via Single-Vat Grayscale Digital Light Processing. *Advanced Functional Materials* 2022, **32**(28)**:** 2112329.

12. Ehrmann K, Barner-Kowollik C. Colorful 3D Printing: A Critical Feasibility Analysis of Multi-Wavelength Additive Manufacturing. *Journal of the American Chemical Society* 2023, **145**(45)**:** 24438-24446.

13. Truong VX, Ehrmann K, Seifermann M, Levkin PA, Barner-Kowollik C. Wavelength Orthogonal Photodynamic Networks. *Chemistry – A European Journal* 2022, **28**(25)**:** e202104466.

14. Dolinski ND, Callaway EB, Sample CS, Gockowski LF, Chavez R, Page ZA*, et al.* Tough Multimaterial Interfaces through Wavelength-Selective 3D Printing. *ACS Applied Materials & Interfaces* 2021, **13**(18)**:** 22065-22072.

15. Cazin I, Gleirscher MO, Fleisch M, Berer M, Sangermano M, Schlögl S. Spatially controlling the mechanical properties of 3D printed objects by dual-wavelength vat photopolymerization. *Additive Manufacturing* 2022, **57:** 102977.

16. Sampson KL, Deore B, Go A, Nayak MA, Orth A, Gallerneault M*, et al.* Multimaterial Vat Polymerization Additive Manufacturing. *ACS Applied Polymer Materials* 2021, **3**(9)**:** 4304-4324.

17. Schwartz JJ, Boydston AJ. Multimaterial actinic spatial control 3D and 4D printing. *Nature Communications* 2019, **10**(1)**:** 791.

18. Dolinski ND, Page ZA, Callaway EB, Eisenreich F, Garcia RV, Chavez R*, et al.* Solution Mask Liquid Lithography (SMaLL) for One-Step, Multimaterial 3D Printing. *Advanced Materials* 2018, **30**(31)**:** 1800364.

19. Rossegger E, Strasser J, Höller R, Fleisch M, Berer M, Schlögl S. Wavelength Selective Multi-Material 3D Printing of Soft Active Devices Using Orthogonal Photoreactions. *Macromolecular Rapid Communications* 2023, **44**(2)**:** 2200586.

20. Chin KCH, Ovsepyan G, Boydston AJ. Multi-color dual wavelength vat photopolymerization 3D printing via spatially controlled acidity. *Nature Communications* 2024, **15**(1)**:** 3867.

21. Wu X, Ehrmann K, Gan CT, Leuschel B, Pashley-Johnson F, Barner-Kowollik C. Two Material Properties from One Wavelength-Orthogonal Photoresin Enabled by a Monochromatic Laser Integrated Stereolithographic Apparatus (Mono LISA). *Adv Mater* 2025, **n/a**(n/a)**:** e2419639.

22. Göschl M, Laa D, Ahmadi M, Koch T, Stampfl J, Ehrmann K*, et al.* Trapping crystallinity in highly crosslinked thermosets by light-based 3D printing from the liquid crystalline phase. *ChemRxiv* 2024, **Preprint**.

23. Herbert KM, Fowler HE, McCracken JM, Schlafmann KR, Koch JA, White TJ. Synthesis and alignment of liquid crystalline elastomers. *Nature Reviews Materials* 2022, **7**(1)**:** 23-38.

24. Fowler HE, Pearl HM, Hoang JD, White TJ. Liquid Crystal Elastomers Prepared by Thiol–Ene Photopolymerization Amenable to Surface-Enforced Alignment. *Macromolecules* 2024, **57**(6)**:** 2619-2627.

25. Białecka-Florjańczyk E, Śledzińska I, Stolarzewicz I, Makal A, Górecka E. Synthesis and study of new liquid crystalline compounds with an epoxy group. *Liquid Crystals* 2009, **36**(1)**:** 67-73.

26. Wu J, Yao S, Zhang H, Man W, Bai Z, Zhang F*, et al.* Liquid Crystal Elastomer Metamaterials with Giant Biaxial Thermal Shrinkage for Enhancing Skin Regeneration. *Advanced Materials* 2021, **33**(45)**:** 2106175.

27. Defize T, Riva R, Raquez J-M, Dubois P, Jérôme C, Alexandre M. Thermoreversibly Crosslinked Poly(ε-caprolactone) as Recyclable Shape-Memory Polymer Network. *Macromolecular Rapid Communications* 2011, **32**(16)**:** 1264-1269.

28. Imae I, Tsukimori M, Fujimoto T, Tsukiyama K, Harima Y. Orientation control of anchored molecules on metal-oxide substrates. *Inorganic Chemistry Communications* 2017, **82:** 44-47.